PHOTONIC SENSORS / Vol. 16, No. 2, 2026: 9560014

Temperature-Compensated and Sensitivity-Enhanced Biosensor for the Detection of EGFR Exon-20 Gene in Non-Small Cell Lung Cancer

Ruyue SHI[1], Hailiang CHEN[1*], Xuan ZHANG[1], Xianyi WANG[1], Shuo LIU[2], Shuguang LI[1], and Sigang YANG[3]

[1]*State Key Laboratory of Metastable Materials Science & Technology; Key Laboratory for Microstructural Material Physics of Hebei Province, School of Science, Yanshan University, Qinhuangdao 066004, China*

[2]*Hebei Key Laboratory of Advanced Laser Technology and Equipment, Tianjin 300401, China*

[3]*Department of Electronic Engineering; Beijing National Research Center for Information Science and Technology, Tsinghua University, Beijing 100190, China*

[*]Corresponding author: Hailiang CHEN E-mail: hlchen@ysu.edu.cn

Abstract: Ultrasensitive detection of the epidermal growth factor receptor (EGFR) gene in non-small cell lung cancer (NSCLC) remains a critical challenge for early diagnosis and targeted therapy. While fiber-optic biosensors offer promising sensing capabilities, their performance is fundamentally limited by the temperature fluctuation and insufficient limit of detection (LOD). In this work, an approaching 4-fold amplification of EGFR-binding spectral shifts is achieved through the Vernier effect (VE) in the cascaded Sagnac interferometer (SI) and Mach-Zehnder interferometer (MZI), whose free spectral ranges (FSRs) are deliberately mismatched. Temperature compensation is achieved through a contour-based differential demodulation method enabled by integrating a fiber Bragg grating (FBG) into the biosensor, which effectively decouples temperature variations from the deoxyribonucleic acid (DNA) molecular hybridization signals. Functionalized with mercaptoethylamine (MEA)-mediated self-assembled monolayers and single-stranded probe DNA (pDNA) specific to the EGFR gene, the biosensor achieves 53.7-fold specificity discrimination with the 25.159 3 nm wavelength redshift for complementary DNA (cDNA) versus 0.468 3 nm for non-complementary DNA (nonDNA), caused by refractive index (RI) changes resulting from DNA hybridization between pDNA and cDNA. The biosensor achieves a prominent LOD of 0.033 63 pM for the synthetic EGFR gene in the buffer, surpassing existing interferometric biosensors by four orders of magnitude. This work not only establishes a new paradigm for overcoming the temperature drift in photonic biosensing but also employs the VE to significantly enhance the LOD, offering transformative potential for early diagnosis of NSCLC in clinical settings.

Keywords: Temperature compensation; non-small cell lung cancer; Vernier effect; fiber Bragg grating; detection of limit

Citation: Ruyue SHI, Hailiang CHEN, Xuan ZHANG, Xianyi WANG, Shuo LIU, Shuguang LI, *et al*., "Temperature-Compensated and Sensitivity-Enhanced Biosensor for the Detection of EGFR Exon-20 Gene in Non-Small Cell Lung Cancer," *Photonic Sensors*, 2026, 16(2): 9560014.

Received: 8 November 2025 / Revised: 24 December 2025

DOI: 10.26599/PhoS.2026.9560014
Article type: Research article

1. Introduction

Lung cancer stands as the leading cause of cancer-related mortality worldwide, where early diagnosis is critical for improving patient survival rates [1, 2]. Non-small cell lung cancer (NSCLC) accounts for 85% of lung cancer cases, with approximately 50% of these cases driven by epidermal growth factor receptor (EGFR) gene mutations, notably exon-19 deletions, exon-20 insertions, and exon-21 L858R point mutations [3, 4]. Each mutation subtype dictates distinct therapeutic strategies, and crucially, exon-20 variants may confer resistance to EGFR tyrosine kinase inhibitors (EGFR-TKIs), the primary targeted therapy. Consequently, specific detection of exon-20 gene fragments is essential for guiding precision treatment in NSCLC [5, 6].

Although current EGFR mutation detection platforms for NSCLC patients, including peptide nucleic acid-locked nucleic acid (PNA-LNA) polymerase chain reaction (PCR) clamp, denaturing high-performance liquid chromatography (dHPLC), scorpion amplified refractory mutation system technology (SARMS), and nano-fluidic digital PCR arrays [7–11] achieve clinical utility, their practical implementation is constrained by fundamental limitations that include reliance on sophisticated instrumentation, prolonged processing times, and unsustainable operational costs, all of which hinder deployment in resource-limited settings. In contrast, label-free optical fiber gene biosensors offer distinct advantages including compact structure, high sensitivity, electromagnetic interference immunity, real-time in situ detection capability, multiplexing potential, and low operational costs, which confer unique benefits for detecting EGFR exon-20 gene fragments [12–15]. Various fiber-optic sensing schemes, such as the fiber Bragg grating (FBG) [16], surface plasmon resonance (SPR) [17–19], and fiber optic interference [20], have been demonstrated for label-free genetic analysis. Due to the weak coupling effect between the outside small deoxyribonucleic acid (DNA) biomolecules and the interior engraving grating, FBG-based biosensors exhibit limited sensitivity. In contrast, SPR-based biosensors depict high sensitivity, but exhibit the large full width at half maximum (FWHM) that obscures low-concentration signals. The unique architecture of the Mach-Zehnder interferometer (MZI) enhances its sensitivity to biomolecular interactions during light propagation through optical fibers, making it particularly well-suited for genetic sensing applications. Liu *et al*. developed a novel biosensor system that integrated an MZI biosensor with isothermal solid-phase DNA amplification (IDA) technology to achieve rapid (30 min) EGFR mutation detection with high sensitivity (1% of mutant allele) and excellent accuracy [21]. Li *et al*. [22] have developed a hybrid system integrating dual SPR and MZI signals for the detection of temperature, pH, and EGFR exon-20, exhibiting a detection limit of 3.27 nM. These results demonstrate that the limit of detection (LOD) for EGFR exon-20 variants remains suboptimal and requires further improvement.

However, a critical roadblock hindering clinical application is that the inherent thermo-optic and thermal expansion coefficients of optical fiber materials induce the significant signal drift under ambient temperature fluctuations, confounding biomolecular binding signals and compromising detection reliability. Current strategies to address temperature crosstalk include maintaining a stable temperature environment or employing dual-parameter biosensors with inherent temperature compensation mechanisms. Maintaining a uniform temperature environment is often impractical in real-world applications, making dual-parameter biosensors a more viable solution. Despite advances in biosensing technologies, the development of

temperature self-compensating biosensors capable of achieving high sensitivity and reliability remains a critical unmet need.

To overcome these limitations and enable precise detection of EGFR exon-20 gene variants, we construct a temperature-compensated biosensing platform based on the Vernier effect (VE) that cascades a Sagnac loop, which contains a 36 cm polarization-maintaining fiber (PMF) and an FBG, and an MZI fabricated using a 6.574 mm taper single mode fiber (TSMF). While both the FBG and envelope formed by the VE exhibit temperature sensitivity, the envelope responds specifically to DNA hybridization-induced refractive index (RI) changes, whereas the FBG serves as a temperature compensation element. By employing a contour-based demodulation method, temperature-induced interference in DNA hybridization detection can be effectively eliminated. The mercaptoethylamine (MEA) functionalization protocol enables robust probe DNA (pDNA) immobilization via NH_2–COOH covalent bonding. This strategy achieves excellent discrimination against fully non-complementary sequences DNA (nonDNA), demonstrating a 53.7-fold specificity contrast and a 25.159 3 nm redshift for complementary DNA (cDNA) compared to only 0.468 3 nm for non-complementary DNA (nonDNA). The use of a fully non-complementary sequence is intended to demonstrate the fundamental specificity of the platform that does not respond to entirely unrelated sequences. This establishes the critical first tier of specificity required for subsequent single-base mismatch resolution. By achieving single-base mismatch resolution, this strategy demonstrates a 53.7-fold specificity contrast between complementary DNA (cDNA) and non-complementary DNA (nonDNA) sequences, which is the 25.159 3 nm redshift of cDNA versus 0.468 3 nm for nonDNA. The temperature-compensated DNA biosensor attains an LOD of 0.033 63 pM, surpassing conventional interferometric biosensors by four orders of magnitude.

2. Experimental setup and operation principles

2.1 Experimental setup

The temperature-compensated biosensor platform based on the VE comprises a cascaded Sagnac loop and an MZI, as illustrated in Fig. 1(a). The Sagnac loop incorporates a 36 cm PMF with an FBG, while the MZI is fabricated using a 6.574 mm TSMF. The light emitted from a broadband source (BBS) (SLED, Shanghai Aoshow Information Technology Co., Ltd., China) is first split by a 1×2 coupler, routing one beam to the Sagnac interferometer (SI) while propagating the other through the TSMF, whose fabrication process and morphological characteristics are illustrated in Figs. 1(b)–1(c). Following this, the optical signals are recombined through a 2×1 coupler, which constitutes the final stage of the process, before being directed to the optical spectrum analyzer (OSA) (YOKOGAWA, AQ6370D, Japan) for data recording and subsequent analysis. With the MZI serving as the sensing arm and the SI as the reference arm, the experimentally measured free spectral ranges (FSRs) are 22.63 nm for the MZI and 17.7 nm for the SI, as derived from Fig. 1(f). The envelope spectrum is then generated by superimposing the interference spectra of the MZI and SI, which have slightly mismatched FSRs, and its scale is calculated using (1) [23]:

$$\mathrm{FSR}_{\mathrm{Envelope}} = \frac{\mathrm{FSR}_{\mathrm{Sen}} \times \mathrm{FSR}_{\mathrm{Ref}}}{\left|\mathrm{FSR}_{\mathrm{Sen}} - \mathrm{FSR}_{\mathrm{Ref}}\right|} \tag{1}$$

where $\mathrm{FSR}_{\mathrm{Envelope}}$ denotes the FSR of the envelope formed by the superposition of the two optical paths, $\mathrm{FSR}_{\mathrm{Sen}}$ represents the FSR of the reference path for SI, and $\mathrm{FSR}_{\mathrm{Ref}}$ indicates the FSR of the sensing path for the MZI. The FSR of the envelope calculated from (1) is 81.25 nm, which is in close agreement with the experimentally measured value of 79.48 nm, as shown in Fig. 1(f). Figures 1(f-1) to 1(f-3) show

the SI spectrum, the MZI spectrum, and the resulting envelope spectrum formed by their superposition, respectively. The loss of the biosensor formed by cascading the MZI based on the TSMF and the SI based on the PMF is 11.735 dB, and the fringe visibility of the resulting envelope spectrum is 0.984. Figure 1(d) depicts the interference spectrum of air and the spectrum of water generated by the TSMF. During the tapering process where a standard SMF with the 125 μm cladding diameter is drawn into a 6.574 mm long TSMF, the resulting SMF and TSMF, whose microscopic schematic diagrams are observed by using a microscope (TMM-500, Tiansheng Inc., China), are shown in Figs. 1(e-1)–1(e-3). Figures 1(g)–1(h) illustrate schematic diagrams of the PMF and FBG incorporated into the Sagnac loop, where the FBG, functioning as a temperature compensation device, exhibits a temperature-dependent shift in its reflection peak, as shown in Fig. 1(h-1). The system employs the TSMF as the functionalized sensing arm and the SI as the stable reference arm. Biomolecular interactions on the TSMF surface induce measurable shifts in the envelope formed at the 2×1 coupler output, enabling real-time detection, as shown in Figs. 1(i)–1(k).

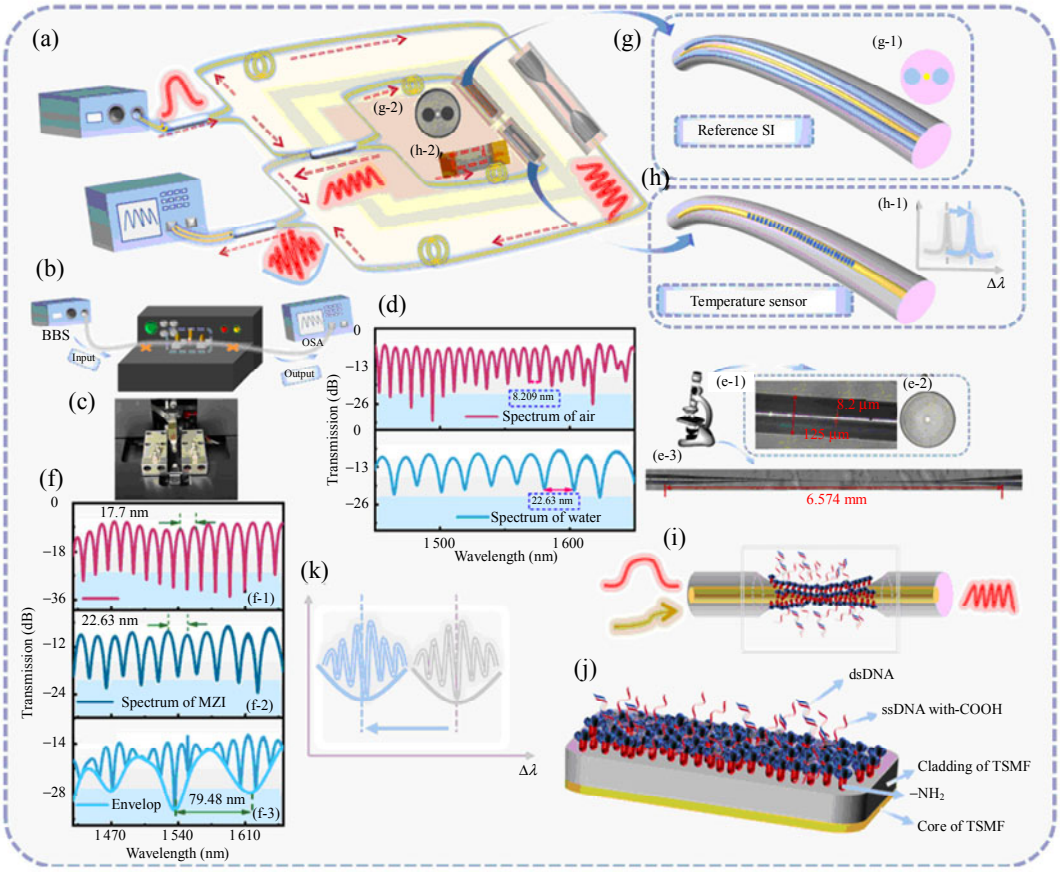

Fig. 1 Temperature-compensated EGFR exon-20 gene biosensor based on the VE: (a) the system architecture integrating VE and FBG, the tapering machine of (b) the schematic diagram and (c) image of the flame head, (d) the spectrum of the MZI, among (d-1) spectrum with air as the background RI and (d-2) spectrum with water as the background RI, (e) micrographs of the sensor, including (e-1) the SMF, (e-2) the end face of the SMF, and (e-3) the TSMF, (f) spectra, including (f-1) the SI, (f-2) the MZI, and (f-3) the envelope, (g) the schematic diagram of the PMF among (g-1) the schematic diagram of the end face of the PMF and (g-2) the micrograph of the end face of the PMF, (h) the schematic diagram of the FBG, among (h-1) the schematic diagram of the FBG shift and (h-2) the physical image of the FBG, (i) the schematic diagram of the biosensor probe, and the schematic diagram of (j) optical fiber surface functionalization and (k) the shift of the envelope.

2.2 Operation principles

Finite element method simulations of polarization (pol) of light in the SMF and TSMF cores, as illustrated in Figs. 2(a), 2(b), 2(g) and 2(h), demonstrate stark modal contrasts. Light remains tightly confined within the SMF core across both transverse axes, while the TSMF core permits significant evanescent leakage into the cladding. Meanwhile, modal analysis is performed on the PMF with its *X*-polarization and *Y*-polarization presented in Figs. 2(d) and 2(e). Due to the presence of stress rods, the PMF exhibits a birefringence (B) of 3.21×10^{-4}, as shown in Figs. 2(f) and 2(c). To further analyze the transmission process of the MZI, we simulate single wavelength (1 550 nm) energy transport using the beam propagation theory. The resulting propagation profile and interference fringe pattern, as illustrated in Figs. 2(i) and 2(j), confirm that the tapered geometry selectively enhances higher-order mode generation, which is a critical mechanism for achieving high RI sensitivity.

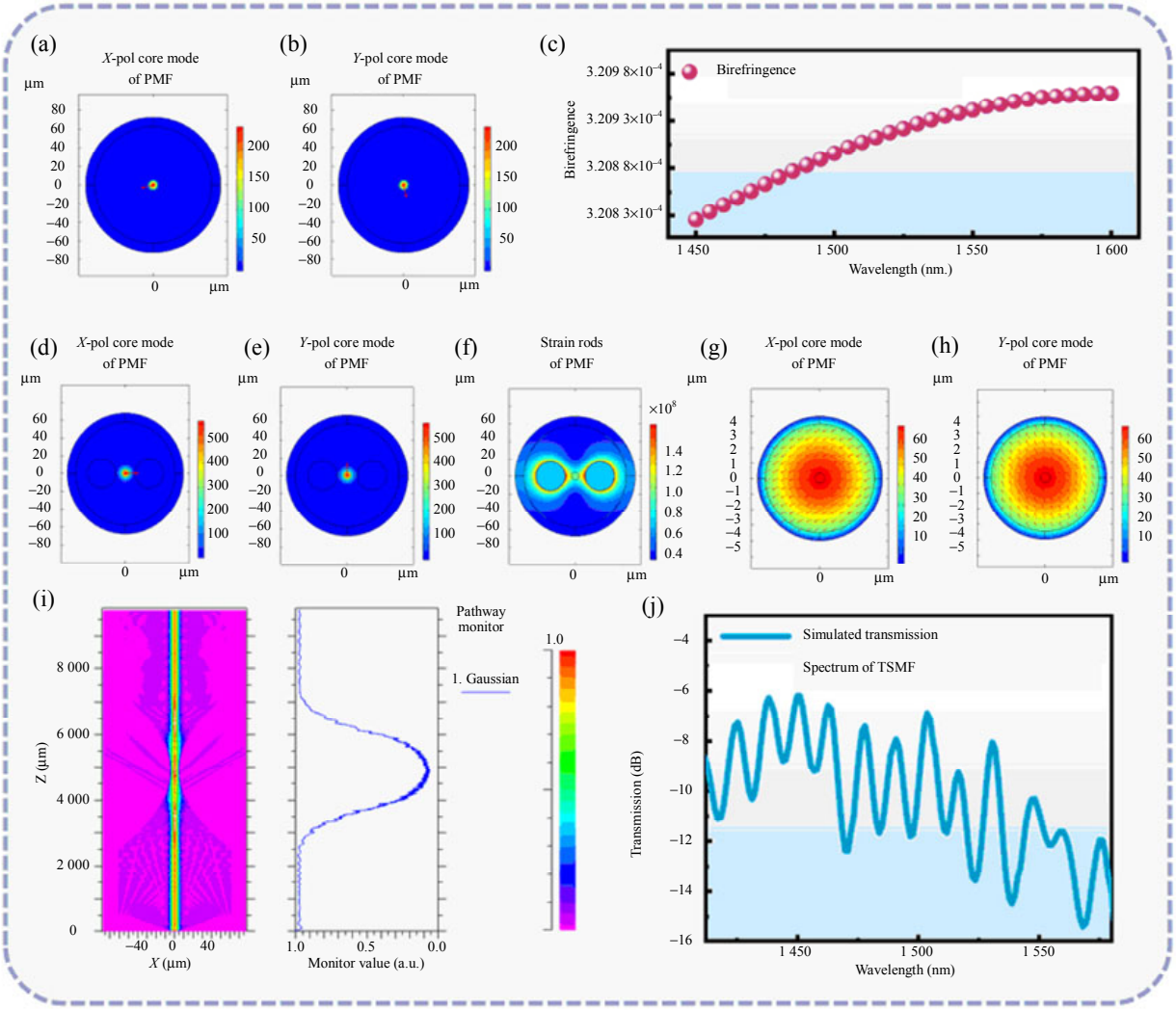

Fig. 2 Simulation calculation of the system structure: fundamental mode of the (a) *X*-direction and (b) *Y*-direction in the standard SMF, (c) birefringence of the PMF; the fundamental mode of the (d) *X*-direction and (e) *Y*-direction in the PMF, (f) the strain distribution of the PMF; the fundamental mode of the (g) *Y*-direction and (h) *X*-direction in the TSMF, (i) simulated mode evolution in the TSMF using the beam propagation theory, and (j) the calculated interference spectrum in the TSMF.

When Δn_{eff} represents the difference in the effective RI between the fundamental mode and the higher-order cladding mode, the MZI formed by these modes can be expressed as [24]

$$I_{\mathrm{MZI}} \propto J_1 J_2 \left(2+2\cos\frac{2\pi\Delta n_{\mathrm{eff}} L_M}{\lambda}\right) \tag{2}$$

when light passes the SI, the intensity of output light can be indicated as

$$I_{\mathrm{SI}} \propto J^2 \left(2+2\cos\frac{2\pi B L_S}{\lambda}\right) \tag{3}$$

where J, J_1, and J_2 represent the magnitudes of the electric fields of the PMF and the cladding and core of the TSMF, respectively, $\Delta\varphi=2\pi\Delta n_{\mathrm{eff}}\ L_S/\lambda$ is the phase of the interference spectrum. L_S and L_M are the lengths of the PMF and TSMF.

The final output light intensity of the cascaded structure, which is the superposition of the intensities of the MZI and the SI, can be obtained as

$$I_{\mathrm{MZI+SI}} \propto \frac{1}{2} A_1 A_2 \left(\sqrt{2+\mathrm{e}^{\mathrm{i}\varphi}+\mathrm{e}^{-\mathrm{i}\varphi}}\right)^2 (\mathrm{e}^{\mathrm{i}\frac{2\pi}{\lambda}n_{\mathrm{core}}L_M}+\mathrm{e}^{\mathrm{i}\frac{2\pi}{\lambda}n_{\mathrm{core}}L_M})(\mathrm{e}^{-\mathrm{i}\frac{2\pi}{\lambda}n_{\mathrm{core}}L_M}+\mathrm{e}^{-\mathrm{i}\frac{2\pi}{\lambda}n_{\mathrm{core}}L_M}) \tag{4}$$

where $A_1\sqrt{2+\mathrm{e}^{\mathrm{i}\varphi_1}+\mathrm{e}^{-\mathrm{i}\varphi_1}}$ and $A_2\sqrt{2+\mathrm{e}^{\mathrm{i}\varphi_1}+\mathrm{e}^{-\mathrm{i}\varphi_1}}$ are the electrical field intensity of the two beams; $\varphi_2=2\pi/\lambda(n_{\mathrm{clad}}-n_{\mathrm{core}})$ represents the phase difference generated from the MZI. It can be deduced as

$$I_{\mathrm{MZI+SI}} \propto 8A_1^2A_2^2\left\{\frac{1}{2}\cos\left[\frac{\pi}{\lambda}(n_{\mathrm{clad}}-n_{\mathrm{core}})L_M-\frac{\pi}{\lambda}BL_S\right]+\frac{1}{2}\cos\left[\frac{\pi}{\lambda}(n_{\mathrm{clad}}-n_{\mathrm{core}})L_M+\frac{\pi}{\lambda}BL_S\right]\right\}^2. \tag{5}$$

3. Results and discussion

3.1 Measurement of the RI

The DNA molecular sensing capability of the biosensor is evaluated through its RI response at first. Figure 3(a) illustrates the preparation method of solutions used to evaluate the biosensor performance, where glucose samples of different masses are weighed and diluted with distilled water to obtain solutions with varying RI. First, we evaluate the RI response of the MZI formed by the TSMF without a cascaded SI, as shown in Figs. 3(b)–3(c). The interference valley exhibit a linear redshift with increasing RI, achieving the sensitivity of 5 438.59 nm/RIU and a fitting coefficient (R^2) of 0.998. Next, we evaluate the RI response of the envelope formed by the cascaded MZI and SI, as shown in Figs. 3(d) and 3(e). The envelope exhibits a linear blueshift with increasing RI, achieving the sensitivity of −18 083.02 nm/RIU with an R^2 of 0.997. A direct comparison between the sensitivity of the cascaded sensor and that of the sensor based on the MZI yields an amplification factor (M) of 3.33. As the sensitivity is amplified due to the VE, the amplification factor M can also be calculated using the following formula:

$$M=\frac{\mathrm{FSR}_{\mathrm{Ref}}}{\left|\mathrm{FSR}_{\mathrm{Sen}}-\mathrm{FSR}_{\mathrm{Ref}}\right|}. \tag{6}$$

We substitute the experimentally measured envelope FSR of 79.48 nm, the sensing arm FSR of 17.7 nm, and the reference arm FSR of 22.63 nm into (2), yielding an amplification factor of 3.6 for the sensor based on the VE. Furthermore, the temperature compensation device shows no significant shift with varying RI, confirming its role as a temperature reference, as illustrated in Fig. 3(f). Figure 3(h) illustrates the schematic diagram of temperature compensation, where both the sensing arm and the FBG need to be placed into the temperature-controlled chamber simultaneously during temperature detection. Heating from 34 ℃ to 45 ℃ induces a redshift of both the envelope and the FBG, as shown in Figs. 3(i) and 3(j). The temperature-dependent response of the envelope is fitted to the equation y=11.063x+1 117.644 with an R^2 value of 0.999, while the FBG transmission dip followed the equation y=0.022 8x+1 548.991, with an R^2 of 0.996, as shown in Fig. 3(k). The temperature is determined from the position of the FBG transmission peak, whereas the specific point on the contour map, identified by the location of the envelope, corresponds to an RI that is derived using the color scale on the right-hand axis, as depicted in Fig. 3(l).

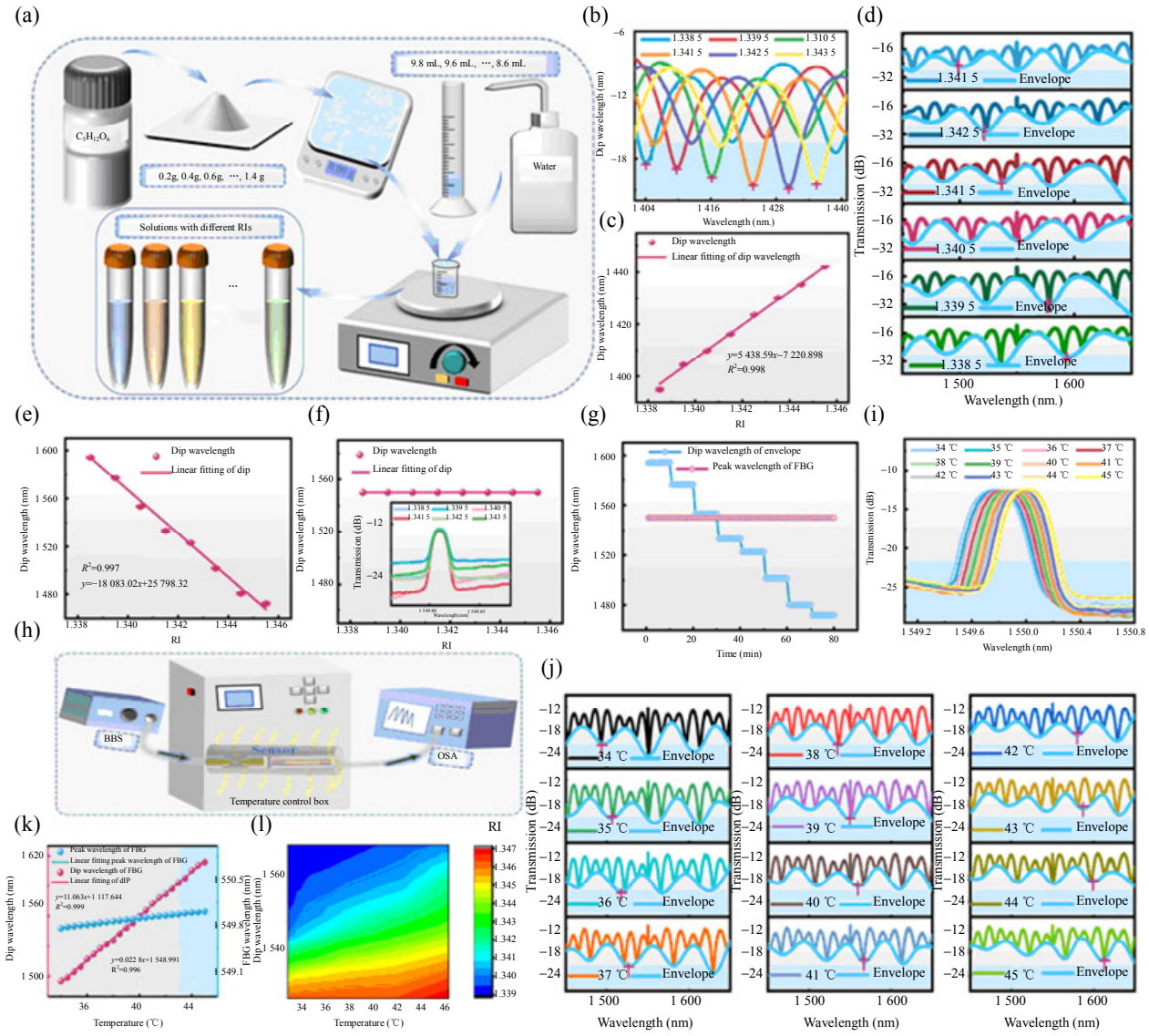

Fig. 3 Temperature compensated RI detection: (a) the preparation method of RI solutions, (b) transmission spectra of the MZI as RI increases from 1.338 5 to 1.343 5, (c) linear fitting of the MZI valleys versus RI, (d) envelopes as RI increases from 1.338 5 to 1.341 5, (e) linear fitting of the envelope versus RI, (f) the change of the FBG, (g) the stability test, (h) the schematic diagram of temperature measurement, the shift of the (i) FBG and (j) envelopes as temperature increases from 34 ℃ to 45 ℃, (k) the linear fitting of the envelopes and FBG versus temperature, and (l) the contour for the demodulation of the temperature and RI.

3.2 DNA hybridization detection

3.2.1 Fabrication of the DNA detection probe

The DNA oligonucleotide (Shanghai Sangon Biotech Co., Ltd., China) and phosphate-buffered saline (PBS, pH=7.4) solutions (Hunan BKMAN Holding Co., Ltd., China) are stored at −20 ℃.

All DNA sequences include pDNA, nonDNA, and EGFR complementary DNA (cDNA). All samples used in this study are synthetically produced by a biotech company and are not collected from human or animal subjects. The base sequence is as follows:

pDNA: 5'-HOOC-CAG GCG GCA CAC GTG GGG GTT GTC CAC GCT-3';

EGFR exon-20: 5'-AGC GTG GAC AAC CCC CAC GTG TGC CGC CTG-3';

nonDNA: 5'-GCG ATG AGC GCA GCG ATA CGT-3'.

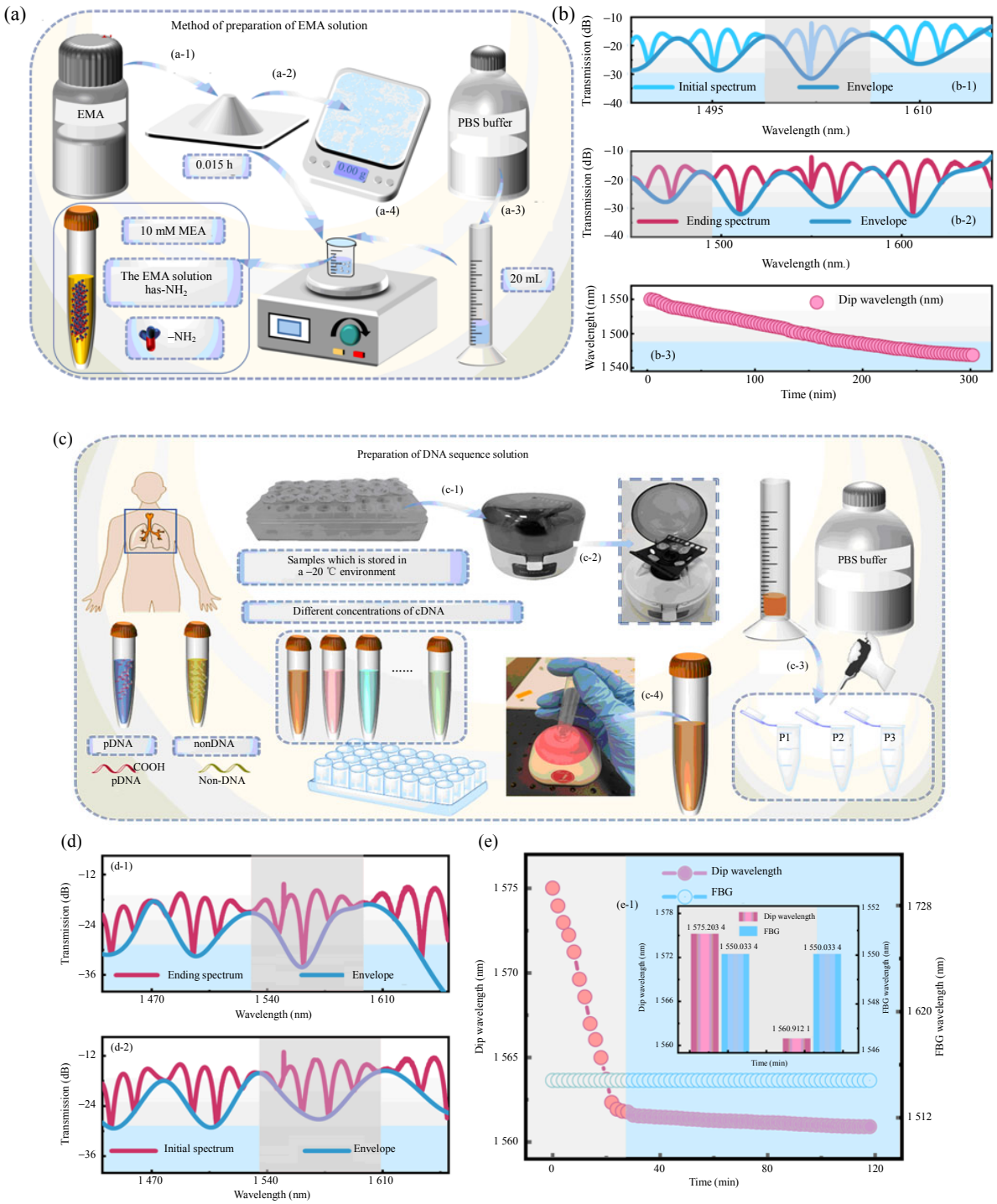

Fig. 4 Processes of functionalization: (a) the preparation process of mercaptoethylamine (MEA) solution, (b) the shift of envelope as fiber is immersed in the MEA solution for 300 min, among (b-1) initial position of the envelope, (b-2) final position and (b-3) the real-time position of the envelope, (c) the preparation of solutions with different DNA sequences, (d) the shift of envelope as the pDNA sequence attaches, among (d-1) initial position and (d-2) final position, and (e) the real-time position of the envelope as the pDNA sequence attaches, among (e-1) the bar chart showing the initial and final positions of the envelope.

Specifically, the pDNA and EGFR exon-20 are completely compatible with each other. A stable duplex region can be established through the formation of hydrogen bonds between base pairs.

The first step in the proposed functionalization process involves the surface pretreatment of the biosensor's sensing region. The fiber surface is activated prior to modification by sequential rinsing

with deionized water and anhydrous ethanol, which cleans the surface and hydroxylates the silanol groups, making them more amenable to molecular interaction. The amine-functionalization is then accomplished by incubating the sensing region in a mercaptoethylamine (MEA) solution prepared in the PBS buffer in Fig. 4(a). The amine-functionalization is achieved through the physical adsorption and electrostatic self-assembly of an MEA monolayer on the silica surface. The protonated amine groups ($–NH_3^+$) in the MEA at neutral pH can form strong electrostatic interactions with the deprotonated silanol groups ($Si–O^–$) on the fiber surface, leading to a stable, positively charged amine-terminated interface suitable for subsequent DNA immobilization. The biosensor is subsequently rinsed with deionized water to remove non-covalently bound MEA molecules. Following this step, the amine functional groups of the MEA are exposed on the sensor surface, making it amenable for subsequent immobilization [25, 26]. Figures 4(b-1) and 4(b-2) respectively show the initial position of the envelope immediately after immersing the sensing arm in the MEA solution and its final position after 300 min. As illustrated in Fig. 4(b-3), the envelope undergoes a gradual blueshift with the fiber immersion. Once the fiber has been immersed in the MEA solution for a sufficient duration, a sufficient quantity of $–NH_2$ groups will have attached to the fiber surface. Subsequently, the fiber is immersed in a solution containing pDNA sequences with –COOH groups, and the pDNA can be immobilized on the fiber surface through stable NH_2–COOH covalent bonding. Furthermore, physical adsorption between the positively charged MEA and the negatively charged pDNA can also facilitate the functionalization of the iosensor. The preparation of solutions with different DNA sequences is illustrated in Fig. 4(c), where the primers are first centrifuged and then diluted with the PBS buffer. With the attachment of the pDNA sequence, the initial and final positions of the envelope are shown in Fig. 4(d), where Figs. 4(d-1) and 4(d-2) depict the initial position of the envelope upon pDNA sequence attachment and the final position of the envelope two hours after attachment, respectively. With the attachment of the pDNA sequence, the envelope undergoes a significant blueshift and eventually stabilizes, indicating the successful attachment of the pDNA sequence, as shown in Fig. 4(e). As shown in Fig. 4(e-1), the initial position of the envelope spectrum is at 1 575.203 nm when the pDNA sequence begins attaching to the sensor. The spectral shift is monitored over a two-hour immobilization period, during which the envelope undergoes a blueshift and stabilizes at 1 560.912 nm. Throughout this process, the ambient temperature is held constant, and the position of the FBG remained fixed at 1 550.033 nm.

Figure 5(a) shows the entire process of the functionalization and specific detection of the biosensor. The process begins with anhydrous ethanol cleaning of the fiber surface to remove contaminants. Next, MEA grafting is performed by 300 min immersion to anchor $–NH_2$ groups. The third step involves incubating the $–NH_2$ functionalized fiber in a 10 μM pDNA sequence for 2 h, where carboxylation (–COOH modification) of pDNA enables stable NH_2–COOH covalent bonding to the fiber surface. The primary goal in this study is to maximize the density of available hybridization sites on the biosensor surface to ensure saturation of available binding sites on the fiber surface. By using a concentration of 10 μM pDNA, we aim to ensure that the subsequent complementary DNA (cDNA) detection signal is limited by the hybridization event itself and not by an insufficient number of immobilized probes. To validate specificity, a nonDNA sequence with zero homology to pDNA is immobilized, and the shift of the envelope is monitored. Finally, hybridization is induced by introducing the fully cDNA strand, with envelope shifts quantified to confirm target binding.

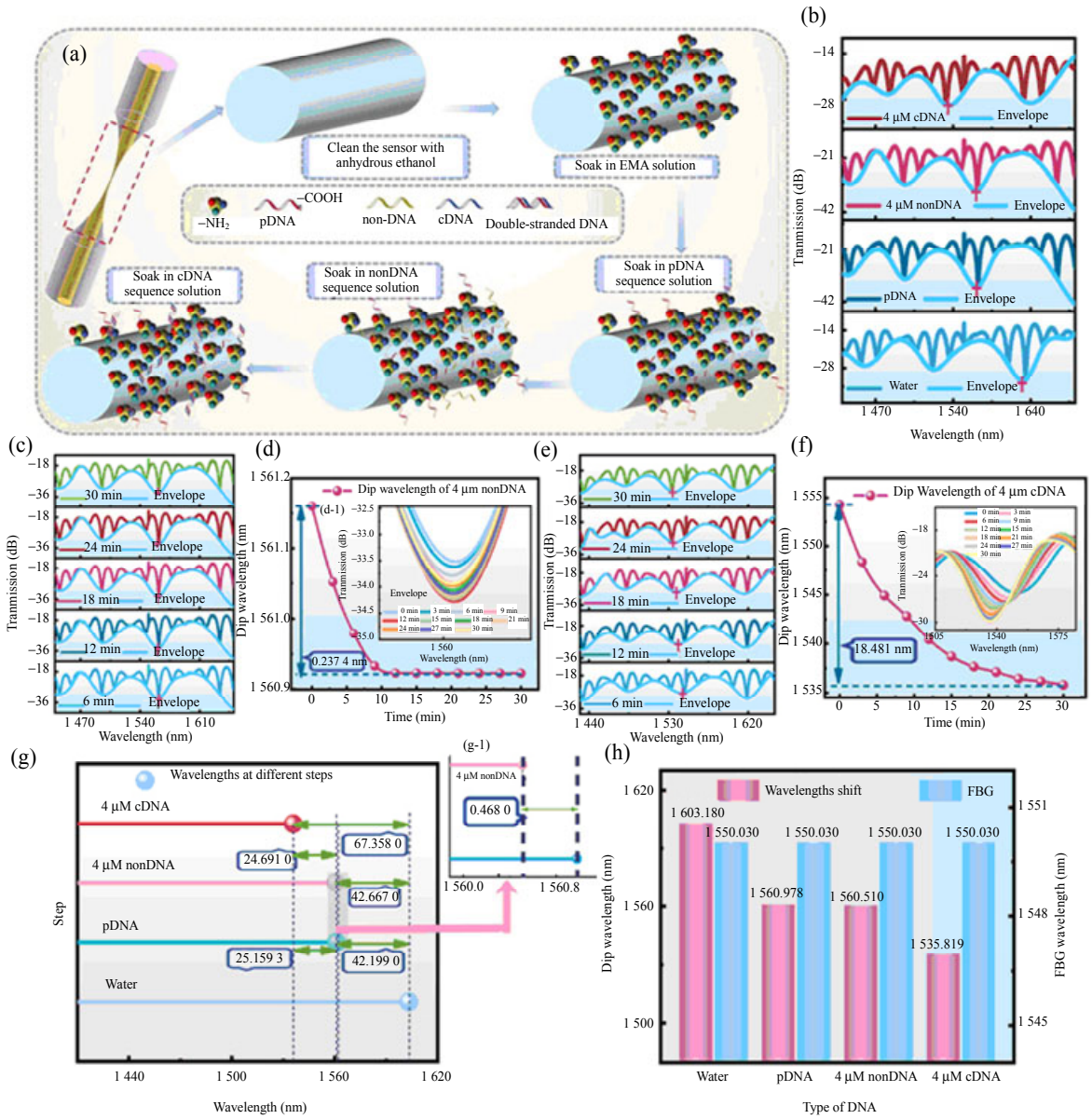

Fig. 5 Specific detection of the DNA biosensor: (a) functionalization steps of the biosensor, (b) the variation in the envelope position when different DNA sequences acting on the optical fiber, (c) the variation in the envelope position within 30 min of nonDNA sequences being applied to the optical fiber, (d) tracking of enveloped locations, among (d-1) the shift of the envelope spectrum, (e) the variation in the envelope position within 30 min of cDNA sequences being applied to the optical fiber, (f) tracking of enveloped locations, among (f-1) the shift of the envelope spectrum, (g) specific shift analysis using a lollipop plot, among (g-1) the enlarged view of the shift of nonDNA relative to pDNA, (h) specific envelope position analysis using a bar chart.

To verify the specificity of the biosensor, two consecutive hybridization experiments are conducted. The cDNA sequence and nonDNA sequence are respectively applied to the optical fiber to observe the variation in envelope shift, as shown in Fig. 5(b). It is evident that the envelope shift induced by the application of cDNA sequences to the optical fiber exhibits a significant blueshift compared with that induced by the nonDNA sequence. Within 30 min of the nonDNA sequence being applied to the optical fiber, a slight blueshift of the envelope occurs, which is attributed to nonspecific interactions, as shown in Figs. 5(c) and 5(d). To clearly observe the spectral shift,

Fig. 5(d-1) displays the variation of the lower envelope alone over the 30 min following the application of the DNA sequence. Evidently, the envelope exhibits no significant displacement. This is because the interaction between the nonDNA molecules and the biosensor surface is weak, likely limited to nonspecific physical adsorption, which does not induce a substantial increase in the surface RI. Within 30 min of cDNA sequences being applied to the optical fiber, a significant blueshift of the envelope occurs and eventually reaches equilibrium. This is due to the hybridization of two complementary DNA strands to form double-stranded DNA (dsDNA), which leads to an increase in the RI on the optical fiber surface, as illustrated in Figs. 5(e) and 5(f). To clearly observe the spectral shift, Fig. 5(f-1) displays the variation of the lower envelope over the 30 min following the application of the cDNA sequence. A distinct blueshift in the envelope spectrum is evident. This occurs because the complementary DNA (cDNA) sequence is a perfect match to the immobilized pDNA, enabling efficient molecular recognition and hybridization. This process forms a stable double-stranded DNA (dsDNA) structure on the biosensor surface. The hybridization event immobilizes a substantial amount of cDNA molecules, significantly increasing the biomolecular mass at the interface and thereby inducing a marked rise in the local RI. The use of a fully non-complementary sequence marks the critical first step in the tiered validation of biosensor specificity. By establishing its ability to discriminate against this entirely unrelated sequence, the fundamental specificity of the biosensor is confirmed, verifying that the proposed platform does not generate false positives. The excellent selectivity achieved in this study lays a solid foundation for the next stage, which is evaluating performance against single and double-base mismatch sequences to ultimately demonstrate its high-resolution and clinically relevant specificity, thereby meeting the requirements for applications such as mutation discrimination.

The displacement analysis of the envelope, as illustrated in Figs. 5(g) and 5(h), reveals the response of the biosensor to different DNA sequences. Initially, with the fiber immersed in water, the envelope is detected at a wavelength of 1 603.18 nm. After immobilizing the pDNA sequence on the fiber surface, a blueshift of the envelope is observed, with the wavelength shifting to 1 560.978 nm and a total envelope shift of 42.199 nm compared to the state where no DNA sequence is present on the optical fiber. This phenomenon is attributed to the increased RI on the fiber surface, which is induced by the attachment of the pDNA sequence. Subsequently, 4 μM nonDNA is attached to the fiber, and the envelope shifts to 1560.51 nm, showing a shift of only 0.468 nm compared to that induced by pDNA, as shown in the magnified view of Fig. 5(g-1) in Fig. 5(g). In contrast, introducing the 4 μM cDNA sequence, specifically binding to the pDNA, induces a more pronounced blueshift, with the envelope shifting to 1 535.819 nm, representing a substantial shift of 25.159 3 nm relative to the pDNA-coated probe. These results highlight the high specificity and sensitivity of the sensor toward the EGFR exon-20 gene and are obtained under a constant-temperature environment, whose maintenance is verified by the fact that the reflection peak of the FBG remains consistently at 1 550.03 nm. An increase in the surface RI following DNA hybridization is analyzed as follows. The densification effect upon duplex formation increases the molecular mass during the transition from single-stranded to double-stranded DNA (dsDNA); consequently, the RI of dsDNA is greater than that of single-stranded DNA (ssDNA) [27]. As the proportion of dsDNA rises, its volume fraction increases significantly, while that of ssDNA decreases correspondingly. This leads to an increase in the average volume fraction of dsDNA and a decrease in ssDNA, with the overall average volume

fraction still showing a net increase. This indicates heightened crowding within the DNA layer as more duplexes form. Therefore, the average RI contributed by dsDNA increases. In other words, the combined effects of structural densification from duplex formation and the increased proportion of dsDNA (indicative of enhanced hybridization) result in a more crowded DNA layer, thereby elevating the average RI at the interface and consequently inducing a phase change in the evanescent field of the propagating photons.

To evaluate the detection limit of the biosensor, cDNA sequences at varying concentrations, which are prepared by serial dilution in the PBS buffer (pH=7.4) to achieve a range from 400 fM to 4 μM including 4 pM, 40 pM, 400 pM, 4 nM, 40 nM, 400 nM, and 4 μM, are applied to the fiber while the envelope response is monitored. Figures 6(a-1)–6(a-8) illustrate the envelope shifts induced by the cDNA sequence at different concentrations, where the envelope gradually undergoes a blueshift with an increase in the cDNA concentration, and this phenomenon is attributed to the specific hybridization between cDNA and pDNA, which increases the RI on the fiber surface. To ensure experimental reliability, the most stable signal is selected for linear regression analysis as depicted in Fig. 6(b), yielding a fitting equation of y=22.054lg$C$+1 604.033 5 (C is the concentration of DNA) with an R^2 value of 0.985 and indicating a strong linear relationship. To enhance the applicability of the sensor for detecting the epidermal growth factor receptor (EGFR) exon-20 gene in NSCLC, we will perform compensation within an ambient temperature range of 29 ℃–44 ℃, close to human body temperature. Figure 6(c) shows the contour plot of our contour-demodulated biosensor. The contour plot is first calibrated using the position of the reflection peak of the FBG to indicate the temperature; the FBG peak position determines the actual temperature during measurement. Then, based on the wavelength of the envelope spectrum on the left axis of the contour plot, the corresponding color in the plot is compared with the color scale bar on the right axis. By matching the colors one-to-one, the concentration of the EGFR exon-20 gene corresponding to the envelope wavelength position is identified. Similarly, when cDNA at different concentrations is applied to the temperature-compensated FBG device, the reflection peak of the FBG remains largely unchanged, as shown in Fig. 6(d). Figure 6(e) further displays the wavelength shift of the FBG reflection peak, demonstrating that it does not vary systematically with changes in the cDNA concentration. The LOD of the biosensor is calculated using the following formula [28]:

$$\mathrm{LOD} = \frac{3\sigma}{S} \tag{7}$$

where σ represents the standard deviation and S denotes the sensitivity. The stability of the biosensor is evaluated by monitoring the stability of the envelope over 100 min, and based on the stability results, the calculated σ value of the sensor is 0.247 26, as shown in Fig. 6(f). Specifically, the inset in Fig. 6(f) shows the variation of the envelope spectrum over a stable 100-min period. By substituting the biosensor sensitivity obtained from Fig. 6(b) and the standard deviation of the noise derived from Fig. 6(f) into (5), the LOD of the biosensor is calculated to be 0.033 63 pM. In conclusion, the LOD improvement is not based on a single mechanism but on a strategic paradigm of signal amplification coupled with the signal-to-noise ratio of the biosensor. Furthermore, long-term monitoring of the envelope demonstrates stable performance in both the wavelength in Fig. 6(g-1) and intensity in Fig. 6(g-2), confirming the robust stability of the biosensor. The stability of the biosensor is evaluated by monitoring the stability of the envelope over 100 min, and based on the stability results, the calculated σ value of the sensor is 0.247 26, as shown in Fig. 6(f). The LOD of the

biosensor is calculated to be 0.033 63 pM according to (5). Long-term monitoring of the envelope demonstrates stable performance in both the wavelength in Fig. 6(g-1) and intensity in Fig. 6(g-2), confirming the robust stability of the biosensor. As shown in Table 1, which presents a performance benchmark of the proposed biosensor against previously reported biosensors based on fiber optical interference, it is evident that the biosensor developed in this study exhibits ultrahigh RI sensitivity that not only achieves an optimization of at least four orders of magnitude in the LOD but also enables simultaneous temperature demodulation.

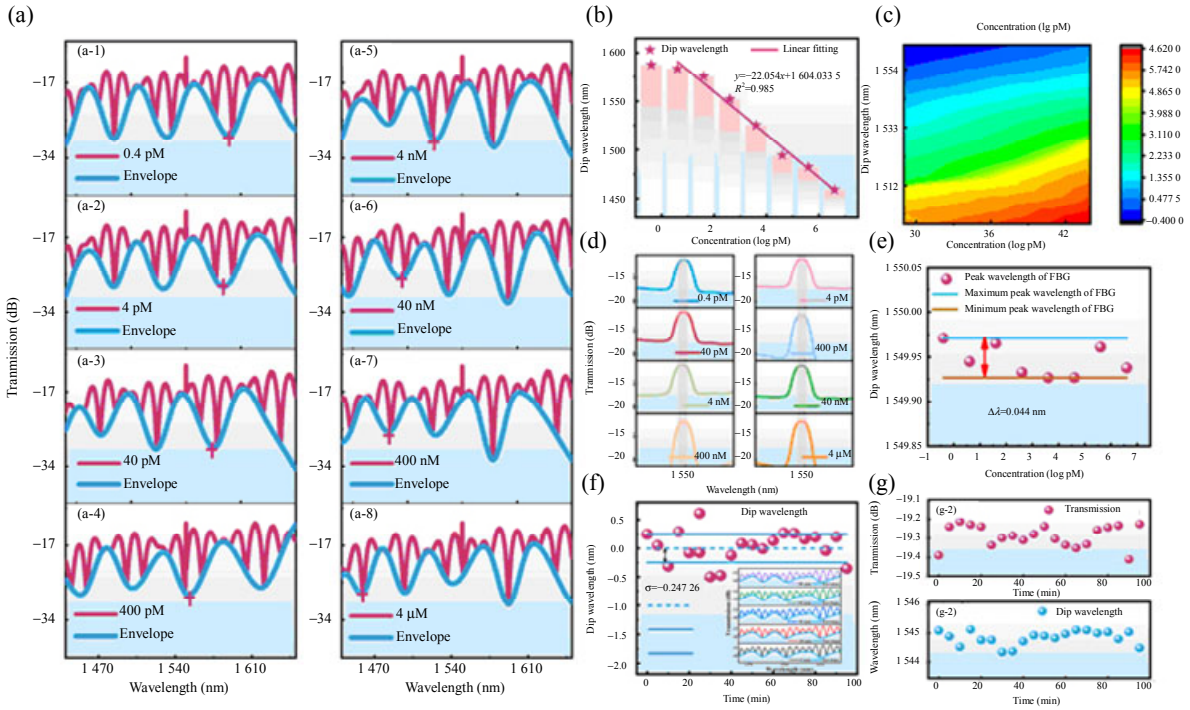

Fig. 6 Evaluation of the LOD: (a) the shift in the envelope with increasing concentration from 400 fM to 4 μM, (b) linear fitting of the envelope and the logarithm of concentration, (c) the contour for the demodulation of the temperature and concentration of DNA, (d) the change of the FBG with the increasing concentration from 400 fM to 4 μM, (e) tracking the reflected peak of the FBG with the increasing concentration from 400 fM to 4 μM, (f) the analysis of the standard deviation, and (g) the analysis of stability.

Table 1 Comparison of the biosensor in our work with other biosensors based on fiber optical interference.

Sensing structure	RI sensitivity (nm/RIU)	Temperature compensated	Detection limit	Reference
FPI+FPI	10 791.12	No	<67.50 nM	[29]
MZI	1 771.00	No	0.31 nM	[30]
MZI	No	No	1.00 nM	[31]
SPR+MZI	No	Yes	3.27 nM	[22]
MZI	No	No	10.00 nM	[32]
MZI	1307.00	Yes	1.87 nM	[26]
SI+MZI	18 083.02	Yes	0.033 63 pM	This work

3.3 Conclusions

In conclusion, we have conceived and experimentally validated a groundbreaking photonic biosensing platform that addresses two perennial bottlenecks in ultrasensitive gene detection, that of pursuing an ultra-low LOD and ensuring measurement reliability under temperature fluctuations. Ingeniously cascading an SI and an MZI with deliberately mismatched FSRs successfully harnesses the VE to amplify the spectral shifts induced by biomolecular binding by a factor of four. More importantly, a contour-based

differential demodulation method that synergistically incorporates an FBG enables complete temperature compensation, thereby effectively isolating the pure hybridization signal of DNA strands from environmental temperature noise. The biosensor demonstrates an outstanding LOD of 0.033 63 pM for the synthetic EGFR gene, a metric that surpasses current interferometric biosensors by four orders of magnitude. The excellent LOD is complemented by an exemplary specificity, achieving a 53.7-fold discrimination factor for the cDNA over the nonDNA sequence. The use of a fully non-complementary sequence marks the critical first step in a tiered validation of sensor specificity. This establishes the platform's ability to discriminate against entirely unrelated sequences, thereby confirming the fundamental specificity of the biosensor and verifying that the proposed sensor platform does not generate false-positive responses. This technology, which enables label-free, highly specific, and thermally stable detection of the EGFR exon-20 gene, holds the strong potential for significant applications in clinical diagnostics by providing a viable path toward improving the early diagnosis of NSCLC and the monitoring of treatment efficacy.

Acknowledgment

The authors would like to thank the Natural Science Foundation of Hebei Province, China (Grant No. F2021203112), National Natural Science Foundation of China (Grant No. 12074331), and Open Project of Hebei Key Laboratory of Advanced Laser Technology and Equipment, China (Grant No. HBKL-ALTE2025006) for help identifying collaborators for this work.

Declarations

Conflict of Interest The authors declare that they have no competing interests.

Permissions All the included figures, tables, or text passages that have already been published elsewhere have obtained the permission from the copyright owner(s) for both the print and online format.

Use of AI Statement None.

References

[1] D. Mathew, M. E. Marmarelis, C. Foley, J. M. Bauml, D. Ye, R. Ghinnagow, *et al*., "Combined JAK inhibition and PD-1 immunotherapy for non-small cell lung cancer patients," *Science*, 2024, 384(6702): eadf1329.

[2] Z. Liu, Z. Yang, J. Wu, W. Zhang, Y. Sun, C. Zhang, *et al*., "A single-cell atlas reveals immune heterogeneity in anti-PD-1-treated non-small cell lung cancer," *Cell*, 2025, 188(11): 3081–3096.E19.

[3] R. Barbara, P. Adelina, and H. Gerhard, "Non-small cell lung cancer-small cell lung cancer transformation as mechanism of resistance to tyrosine kinase inhibitors in lung cancer," *Cancer Drug Resistance*, 2020, 3(2): 171–178.

[4] H. Jeon, S. Wang, J. Song, H. Gill, and H. Cheng, "Update 2025: management of non-small-cell lung cancer," *Lung*, 2025, 203(1): 53.

[5] H. Yasuda, S. Kobayashi, and D. B. Costa, "EGFR exon 20 insertion mutations in non-small-cell lung cancer: preclinical data and clinical implications," *The Lancet Oncology*, 2012, 13(1): e23–e31.

[6] L. V. Sequist, V. A. Joshi, P. A. Jänne, A. Muzikansky, P. Fidias, M. Meyerson, *et al*., "Response to treatment and survival of patients with non-small cell lung cancer undergoing somatic EGFR mutation testing," *The Oncologist*, 2007, 12(1): 90–98.

[7] J. Obradovic and V. Jurisic, "Evaluation of current methods to detect the mutations of epidermal growth factor receptor in non-small cell lung cancer patients," *Multidisciplinary Respiratory Medicine*, 2012, 7(1): 52.

[8] G. Ellison, G. Zhu, A. Moulis, S. Dearden, G. Speake, and R. McCormack, "EGFR mutation testing in lung cancer: a review of available methods and their use for analysis of tumour tissue and cytology samples," *Journal of Clinical Pathology*, 2013, 66(2): 79–89.

[9] S. Dufort, M. J. Richard, S. Lantuejoul, and F. de Fraipont, "Pyrosequencing, a method approved to detect the two major EGFR mutations for anti EGFR therapy in NSCLC," *Journal of Experimental & Clinical Cancer Research*, 2011, 30(1): 57.

[10] S. Simonetti, M. A. Molina, C. Queralt, I. de

Aguirre, C. Mayo, J. Bertran-Alamillo, *et al*., "Detection of EGFR mutations with mutation-specific antibodies in stage IV non-small-cell lung cancer," *Journal of Translational Medicine*, 2010, 8(1): 135.

[11] C. P. O'Brien, S. E. Taylor, J. J. O'Leary, and S. P. Finn, "Molecular testing in oncology: problems, pitfalls and progress," *Lung Cancer*, 2014, 83(3): 309–315.

[12] L. Zhang, Y. Zhen, and L. Tong, "Optical micro/nanofiber enabled tactile sensors and soft actuators: a review," *Opto-Electronic Science*, 2024, 3(8): 240005.

[13] S. Zhang, H. Li, C. Fan, Z. Zeng, C. Xiong, J. Wu, *et al*., "Adaptive decentralized AI scheme for signal recognition of distributed sensor systems," *Opto-Electronic Advances*, 2024, 7(12): 240119.

[14] S. Zhang, H. Chen, H. Li, L. Li, X. Fan, M. Cai, *et al*., "A fiber optic refractive index sensor with temperature compensation based on cascaded Mach-Zehnder interference and intermodal interference," *Measurement*, 2025, 241: 115768.

[15] M. Cai, H. Chen, S. Zhang, S. Jia, M. Gu, J. Hu, *et al*., "Enhanced cryogenic temperature sensor from 320 to 20 K amplified by Vernier effect," *APL Photonics*, 2025, 10(3): 036118.

[16] S. Chen, C. Zhang, J. Wang, N. Li, Y. Song, H. Wu, *et al*., "A fiber Bragg grating sensor based on cladding mode resonance for label-free biosensing," *Biosensors*, 2023, 13: 97.

[17] X. Li, P. Gong, Q. Zhao, X. Zhou, Y. Zhang, and Y. Zhao, "Plug-in optical fiber SPR biosensor for lung cancer gene detection with temperature and pH compensation," *Sensors and Actuators B: Chemical*, 2022, 359: 131596.

[18] T. Liyanage, M. Lai, and G. Slaughter, "Label-free tapered optical fiber plasmonic biosensor," *Analytica Chimica Acta*, 2021, 1169: 338629.

[19] X. Fan, "Sensitive surface plasmon resonance label-free biosensor on a fiber end-facet," *Light: Science & Applications*, 2022, 11(1): 325.

[20] W. Yu, T. Lang, J. Bian, and W. Kong, "Label-free fiber optic biosensor based on thin-core modal interferometer," *Sensors and Actuators B: Chemical*, 2016, 228: 322–329.

[21] Q. Liu, S. Y. Lim, R. A. Soo, M. K. Park, and Y. Shin, "A rapid MZI-IDA sensor system for EGFR mutation testing in non-small cell lung cancer (NSCLC)," *Biosensors and Bioelectronics*, 2015, 74: 865–871.

[22] X. Li, P. Gong, X. Zhou, S. Wang, Y. Liu, Y. Zhang, *et al*., "In-situ detection scheme for EGFR gene with temperature and pH compensation using a triple-channel optical fiber biosensor," *Analytica Chimica Acta*, 2023, 1263: 341286.

[23] Y. Liu, H. Chen, Q. Chen, B. Li, and S. Li, "Experimental study on dual-parameter sensing based on cascaded Sagnac interferometers with two PANDA fibers," *Journal of Lightwave Technology*, 2022, 40(9): 3090–3097.

[24] R. Shi, H. Chen, X. Fan, C. Liu, H. Li, Z. Gao, *et al*., "Highly sensitive strain and temperature sensors based on Vernier effect in cascaded Mach-Zehnder interferometer and Sagnac interferometer," *IEEE Transactions on Instrumentation and Measurement*, 2024, 73: 1–10.

[25] Z. Gao, R. Shi, H. Chen, and L. Li, "Label-free in situ detection of DNA hybridization based on long-range surface plasmon resonance in microstructured optical fiber," *IEEE Transactions on Instrumentation and Measuremen*t, 2025, 74: 1–7.

[26] X. G. Hu, Y. Zhao, Y. Peng, X. M. Chen, L. F. Wang, Z. T. Lin, *et al*., "In-situ label-free temperature-compensated DNA hybridization detection with a fiber-optic interferometer and a fiber Bragg grating for microfluidic chip," *Biosensors and Bioelectronics*, 2023, 242: 115703.

[27] S. Elhadj, G. Singh, and R. F. Saraf, "Optical properties of an immobilized DNA monolayer from 255 to 700 nm," *Langmuir*, 2004, 20(13): 5539–5543.

[28] P. Gong, Y. Wang, X. Zhou, S. Wang, Y. Zhang, Y. Zhao, *et al*., "In situ temperature-compensated DNA hybridization detection using a dual-channel optical fiber sensor," *Analytical Chemistry*, 2021, 93(30): 10561–10567.

[29] F. Li, X. Li, X. Zhou, P. Gong, Y. Zhang, Y. Zhao, *et al*., "Plug-in label-free optical fiber DNA hybridization sensor based on C-type fiber Vernier effect," *Sensors and Actuators B: Chemical*, 2022, 354: 131212.

[30] X. Li, N. Chen, X. Zhou, Y. Zhang, Y. Zhao, L. V. Nguyen, *et al*., "In-situ DNA detection with an interferometric-type optical sensor based on tapered exposed core microstructured optical fiber," *Sensors and Actuators B: Chemical*, 2022, 351: 130942.

[31] X. Zhang, B. Liu, H. Zhang, X. Zhang, B. Song, J. Wu, *et al*., "Label-free detection of DNA hybridization utilizing dual S-tapered thin-core fiber interferometer," *Journal of Lightwave Technology*, 2019, 37(11): 2762–2767.

[32] J. Wu, X. Zhang, B. Liu, H. Zhang, and B. Song, "Square-microfiber-integrated biosensor for label-free DNA hybridization detection," *Sensors and Actuators B: Chemical*, 2017, 252: 1125–1131.